Cobalt location in $p-CoO_xIn-SnO_2$ nanocomposites : correlation with gas sensor performances

Cobalt location in *p*-CoO_x/*n*-SnO_2 nanocomposites: correlation with gas sensor performances

S.A. Vladimirova[1], M.N. Rumyantseva[1*], D.G. Filatova[1], A.S. Chizhov[1], N.O. Khmelevsky[2], E.A. Konstantinova[3,4,5], V.F. Kozlovsky[1], A.V. Marchevsky[6], O.M. Karakulina[7], J. Hadermann[7], A.M. Gaskov[1]

[1]*Chemistry Department, Moscow State University, 119991 Moscow, Russia*

[2]*LISM, Moscow State Technological University Stankin, 127055 Moscow, Russia*

[3]*Physics Department, Moscow State University, 119991 Moscow, Russia*

[4]*Faculty of nano-, bio-, information and cognitive technologies, Moscow Institute of Physics and Technology, 141700 Dolgoprudny, Moscow Region, Russia*

[5]*N. Semenov Institute of Chemical Physics RAS, 119991 Moscow, Russia*

[6]*Department of Materials Science, Moscow State University, 119991 Moscow, Russia*

[7]*EMAT, University of Antwerp, B-2020 Antwerp, Belgium*

ABSTRACT

Nanocomposites CoO_x/SnO_2 based on tin oxide powders with different crystallinity have been prepared by wet chemical synthesis and characterized in detail by ICP-MS, XPS, EPR, XRD, HAADF-STEM imaging and EDX-STEM mapping. It was shown that cobalt is distributed differently between the bulk and surface of SnO_2 nanocrystals, which depends on the crystallinity of the SnO_2 matrix. The measurements of gas sensor properties have been carried out during exposure to CO (10 ppm), and H_2S (2 ppm) in dry air. The decrease of sensor signal toward CO was attributed to high catalytic activity of Co_3O_4 leading to oxidation of carbon monoxide entirely on the surface of catalyst particles. The formation of a *p*-CoO_x/*n*-SnO_2 heterojunction results in high sensitivity of nanocomposites in H_2S detection. The conductance significantly changed in the presence of H_2S, which was attributed to the formation of metallic cobalt sulfide and removal of the *p* – *n* junction.

Keywords: Nanostructured materials; Tin dioxide; Cobalt oxide; P – n heterojunction; Semiconductor gas sensor.

* Corresponding author. Tel. +74959395471 Fax +74959390998 E-mail: roum@inorg.chem.msu.ru

1. Introduction

Low selectivity is one of the principal problems of resistive type gas sensors based on semiconductor metal oxides. From materials science point of view, the solution can be found through the surface modification of highly dispersed semiconductor oxide matrix with clusters of transition metals or their oxides, which may affect the chemical properties of the surface. This method implies a directed change in the chemical state of the surface, the creation of active centers of specific chemical interaction with the target gas simultaneously with a decrease in the concentration of centers of non-selective interaction. Chemical modification leads to a sharper separation of receptor (surface) and transducer (volume) functions in a complex process of sensor signal formation. The effectiveness of this approach to increase the sensitivity and selectivity of sensor materials has already been demonstrated in the literature [1-3].

The distribution of the modifier between the bulk and the surface of crystalline grains of the major phase is very important for the formation of functional properties of the nanocomposites [3]. This is especially important when the main phase and modifier are semiconductors of different conductivity type. The insertion of admixture atoms into the crystalline structure of the *n*-type semiconducting oxide results in the formation of impurity levels, the compensation effect of donor oxygen vacancies by acceptor admixture defects, and the modulation of the band relief of the semiconductor. The segregation of the modifier on the grains surface of the major phase can result in the formation of $p - n$ junctions in the region of intergrain contacts, which also inevitably affects the electrophysical properties of the material. The distribution of the components is given by fundamental characteristics, such as the ionic radii of the corresponding metals, and by the synthesis conditions, mainly by the way of adding a modifier and annealing temperature [3,4].

In nanocomposites based on *n*-SnO_2 and cobalt oxides *p*-CoO or *p*-Co_3O_4 both electronic and chemical sensitization can be realized. Being an additive, cobalt oxides can form solid solutions with SnO_2 (cobalt is located in the volume of the SnO_2 grains) and also segregate at the surface of tin dioxide (cobalt is located on the surface of the SnO_2 crystallites). These variations in Co distribution in the SnO_2 matrix will have different influences on the electrical properties of the materials and their reactivity in the interaction with the gas phase.

The gas sensor properties of nanocrystalline materials based on cobalt-doped tin dioxide were previously investigated [5-10]. It was revealed that this doping can be accompanied by either improvement of sensor parameters at low cobalt concentration levels, or by degradation of sensor characteristics, when the cobalt concentration exceeds its solubility limit in SnO_2 [9]. In this case a part of cobalt atoms not involved in the solid solution can form crystallites of its own phase or segregate on the grain surface of the major phase (SnO_2) as a two dimensional layer, which is not detected by X-ray diffraction. Such a system is similar to supported catalysts, in which the active phase of cobalt oxide is

supported over conventional supports, such as alumina or silica, or over reducible oxides, such as ceria [11]. These materials were intensively studied in the processes of low temperature oxidation of CO [11], and low temperature gas desulfurization [12,13].

Nanoheterogeneous systems based on cobalt and tin oxides in form of three-dimensional nanocomposites [14], core-shell nanospheres [15,16], microreactors [17], nanofibers with different cobalt distribution [18-22] were recently investigated as gas sensitive materials for NH_3, H_2, CO, and volatile organic compounds (VOCs) detection. The obtained results are analyzed in terms of formation of $p - n$ junctions between oxides with different type of conductivity. The interaction of oxygen and target gases with p – and n – parts of these heterojunctions results in the modulation of potential barrier height and formation of increased sensor signal as compared with individual oxides. However, these arguments have general character, do not take into account the chemical nature of target gases, and do not explain the selectivity of the materials in the detection of NH_3 [15], methylbenzenes [16], benzene [17], ethanol [14,19], and acetone [18].

In this paper, we analyze the influence of cobalt location in CoO_x/SnO_2 nanocomposites on their microstructure parameters, electrophysical properties and sensor signal toward CO and H_2S. CO and H_2S are among the main air pollutants. The maximum permissible concentrations of these gases in the working area are 16.2 and 2 ppm, respectively. Both these gases belong to the class of reducing gases, in their presence, the electrical conductivity of *n*-type semiconductor oxides increases. However, they are characterized by different acid properties: CO does not have pronounced acidic or basic properties, while H_2S is an acidic gas. Since cobalt oxide is a catalyst for low-temperature oxidation of CO, and also exhibits activity in the interaction with H_2S, its use for SnO_2 surface modification can provide an increase in tin dioxide selectivity in the detection of CO and H_2S. The gas sensor properties of nanocrystalline materials based on cobalt-doped tin dioxide toward CO were previously investigated [5,6,17,21,22], while gas sensor performance of CoO_x/SnO_2 nanocomposites toward H_2S were considered only in Ref. 22.

To ensure a different distribution of cobalt between the surface and the volume of tin dioxide, the semiconductor matrix was subjected to preliminary temperature treatment at 300 and 750 ^oC. It was shown earlier on the example of the SnO_2-Fe_2O_3 system [3] that low annealing temperature (300 ^oC) makes it possible to obtain solid solutions of a large extent, while the use of a temperature exceeding 700 ^oC, leads to the formation of two-phase oxide systems. Different cobalt distribution was confirmed by independent determination of cobalt content on the surface of the SnO_2 grains and in the SnO_2 crystal structure. Gas sensor performance of CoO_x/SnO_2 materials were analyzed in terms of compensation effect of donor oxygen vacancies by acceptor cobalt defects, the role of the $p – n$ heterojunction in sensor signal formation, and the gas reaction taking place entirely on the surface of catalyst particles.

2. Materials and methods

2.1 Materials synthesis

Tin dioxide powders were prepared by conventional hydrolysis of $SnCl_4$ [23]. A measured amount of $SnCl_4$*$5H_2O$ was dissolved in deionised water in an ice bath and 25% ammonia solution was slowly added to the stirred solution to achieve a complete precipitation of α-stannic acid. The resulting gel was centrifuged, washed with deionised water up to complete removal of the chloride ions ($AgNO_3$ test), dried at 100^{o}C, and annealed at 300 or 750 ^{o}C for 24 hours. After that, the cobalt was introduced with concentration corresponding to X = [Co]/([Co]+[Sn]) = 1.5 – 10 at.% by wetness impregnation procedure using $Co(NO_3)_2$ solution. Then, the powders were dried at 100 ^{o}C and calcined in air at 450 ^{o}C for 24 h.

In accordance with the preassigned atomic cobalt content (X) and annealing temperature of SnO_2 matrix (300 or 750 ^{o}C) the nanocomposites are named as *CoXSn300* or *CoXSn750* (Table 1).

2.2. Materials characterization

High angle annular dark field scanning TEM (HAADF-STEM) images and energy dispersive X-ray spectroscopy (EDX-STEM) maps were acquired at a FEI Tecnai Osiris transmission electron microscope operating at 200 kV. The instrument was equipped with Super-X detectors. The specimens for transmission electron microscopy (TEM) were prepared by dispersing powders in ethanol. A few drops of the resulting dispersion solution were deposited on a copper grid covered with a holey-carbon film.

The sample composition was determined by inductively coupled plasma mass spectrometry (ICP-MS) on a quadrupole ICP mass spectrometer (Agilent 7500c; Agilent Technologies, Germany). Data were acquired and processed with the ICP-MS ChemStation (version G1834B) software package (Agilent Technologies). ^{59}Co, ^{118}Sn and ^{120}Sn isotopes were used for analytical measurements in order to control possible interferences. To determine the Co concentration on the SnO_2 surface the pre-weighed samples were treated with HCl (conc.) and HNO_3 (conc.) (3:1 mixture) in an ultrasonic bath for 15 min. By this, only cobalt oxide was dissolved. Then the supernatant liquid was analyzed. For the estimation of total Co content in the nanocomposites, the powders were pre-weighed and entirely dissolved in HCl (conc.), HNO_3 (conc.) and HF (conc.) (3:1:3 mixture) at 210°C using a microwave system of closed type MARS-5 with pressure vessels XP-1500 Plus (CEM, USA) with the ability to control temperature and pressure. The resulting solutions were diluted 1000 times with high-purity deionized water (Millipore, Bedford, USA) and acidified by adding of 100 μl of 65% nitric acid (Suprapur grade, Merck, Germany). The ICP-MS single element standards (Co, Sn; 10 mg L^{-1}) were products of High Purity Standards (Charleston, USA).

X-ray photoelectron spectroscopy (XPS) measurements were performed using a K-Alpha (Thermo Scientific) spectrometer equipped with a monochromatic Al K_α X-ray source (E = 1486.7 eV). Charge neutralization was applied, providing the C1s peak position of 285.0 eV. XP-spectra were fitted by Gaussian – Lorentzian convolution functions with simultaneous optimization of the background parameters.

EPR spectra were recorded by the standard Bruker EPR spectrometer ELEXSYS-500 (X-band, sensitivity is around ~10^{10} spin/G). The $CuCl_2 \cdot 2H_2O$ reference was used for the calculation of spin center (defect) concentration. The defect concentration was precisely calculated by double integration of experimental EPR spectrum (registered as first derivative of the absorption signal), taking into account background (cavity with empty ampoule). The illumination of the samples was carried out directly inside the cavity of the EPR spectrometer using a high-pressure mercury lamp Bruker ELEXSYS ER203 UV (100 W, spectral range 240÷1000 nm, excitation intensity – 50 mW/cm^2).

Phase composition was determined by X-ray powder diffraction (Rigaku diffractometer, monochromatized Cu $K_{\alpha 1}$ radiation, λ=1.5406 Å). The crystallite size (d_{XRD}) was calculated from the broadening of the most intensive XRD peaks of the SnO_2 (110, d = 3.347 Å) and Co_3O_4 (311, d = 2.437 Å) phases using the Scherrer equation.

The specific surface area (S_{BET}) of the powders was determined by low temperature nitrogen adsorption (BET analysis, Micromeritics Chemisorb 2750).

For the gas sensing experiments, the materials were mixed with a vehicle (α-terpineol in ethanol) and deposited in the form of thick films over functional substrates, having Pt contacts on the front side and a Pt-meander on the back-side, which acts both as a heating element and a temperature probe. The thick films were dried at 30 ^{o}C for 24h and sintered at 450 ^{o}C for 10h in air. All sensor measurements have been carried out by flow-through technique under a controlled constant flux of 100 ml/min. The atmosphere composition was pre-assigned by means of electronic mass-flow controllers (Bronkhorst). The background atmosphere was obtained from a pure air generator. DC volt-amperometric measurements (U = 3 V) have been carried out to monitor the electrical conductance of the sample during exposure to CO (10 ppm), and H_2S (2 ppm) in dry air. The response S of the sensor was calculated as $S = (G_{gas} - G_{air})/G_{air}$, where G_{gas} is the conductance of the sample in the presence of reducing gas, G_{air} is the conductance in pure air.

3. Results and discussion

3.1 Nanostructure characterization

HAADF-STEM images of the *Co10Sn300* and *Co10Sn750* nanocomposites are shown in Fig. 1. Sample *Co10Sn300* (Fig. 1a) consists of 4 – 7 nm nanoparticles. In *Co10Sn750* (Fig. 1b) the

nanoparticles are significantly larger, with a size ranging from 20 to 50 nm. Electron diffraction pattern of *Co10Sn300* (Fig. 1a, inset) consists of broad continuous rings. Observed interplanar spacings approximately correspond SnO_2 structure's ones (Table 2). In case of *Co10Sn750*, rings are more narrow and intermittent (Fig. 1b, inset), which agrees with the fact that nanoparticles in *Co10Sn750* have larger sizes. According to the values of interplanar spacings, this sample contains SnO_2 and Co_3O_4 phases (Table 2).

EDX-STEM mapping was used to distinguish nanoparticles of different composition. In the *Co10Sn300* sample tin and cobalt are uniformly distributed in the nanoparticles (Fig. 2) with a Sn/Co ratio of 90/10 at. %. Assuming that cobalt is in +2 oxidation state, this Sn/Co ratio corresponds to a mass cobalt content of 4.1 wt. %. In contrast to this, in the *Co10Sn750* nanocomposite separate tin- and cobalt-containing oxide particles are present (Fig. 3).

3.2 Composition analysis

The methodology of composition analysis using ICP-MS proposed in this paper made it possible to determine the cobalt content on the surface of SnO_2 grains and in the SnO_2 crystal structure independently from each other. Fig. 4 shows the Co content (wt. %) on the surface of SnO_2 *vs*. its total amount (wt. %) in the samples. In case of the *CoXSn750* nanocomposites both values coincide within the error of analysis, revealing that all cobalt is located on the surface of the SnO_2 crystallites. On the other hand, in the *CoXSn300* nanocomposites the surface cobalt content is about 30% of the total amount of cobalt (Table 1). This indicates that the cobalt distribution between the bulk (crystal structure) and the surface of the SnO_2 nanocrystals depends on the crystallinity of the SnO_2 matrix, which in turn is determined by the annealing temperature.

3.3 Cobalt electronic state analysis

The electronic state of the elements was examined by XPS method (Fig. 5). The positions of the peaks $Sn3d_{5/2}$ (486.6 eV) and $Sn3d_{3/2}$ (495.0 eV) correspond to Sn (IV) [24]. Oxygen in the XP-spectra of the samples exhibits an asymmetric O1s signal. The main peak (530.4 eV) refers to the SnO_2 lattice oxygen anions [24]. The second one (531.7 eV) is due to the presence of various forms of oxygen adsorbed on the SnO_2 surface.

Determination of cobalt oxidation state from XPS data is a difficult task because Co(II) and Co(III) have very similar Co-2p binding energies. However, the Co(II) 2p core level exhibits a strong shake-up satellite peak towards higher binding energy in contrast to Co(III) 2p, which exhibits only a weak satellite [25]. In addition, the separation of the Co $2p_{1/2}$–$2p_{3/2}$ spin-orbit components is about 16.0 eV for Co(II) and 15.0 eV for Co(III). The XP-spectra of the investigated samples in the Co 2p binding energy region are shown in Fig. 6. Depending on total cobalt content in nanocomposites and annealing temperature of SnO_2 matrix, the experimental curves can be fitted by 2 or 4 doublets corresponding to Co(III) and Co(II) main peaks and Co(II) shake-up satellites.

Table 3 presents the Co $2p_{3/2}$ XPS spectral assignments and spin orbit splittings for all obtained samples. By comparison of the estimated Co $2p_{3/2}$ binding energies with reference data [26,27] one can conclude that in nanocomposites *CoXSn300*, synthesized at lower temperature (300^{o}C), cobalt is present in the +2 oxidation state and has an environment corresponding to CoO. In case of samples synthesized at high temperature, *Co10Sn750* nanocomposite have cobalt in oxidation state +2 and +3, wherein the environment of Co(II) meets both the structure of CoO, and Co_3O_4. However, in nanocomposite containing just ~1 wt. % Co *(Co1.5Sn750),* cobalt is only present in the +2 oxidation state as in *CoXSn300* samples.

Additional information about cobalt electronic states was extracted from EPR data. Shown in Fig. 7a, EPR spectra for the *Co5Sn750* and *Co10Sn750* samples comprise an asymmetric broad line (line-width ΔH = 520 G) with *g*-factor g_{eff} = 2.23. According to the literature data [28-30], the EPR signal with such parameter is attributed to Co^{2+} ions in Co_3O_4 based structures. Due to the absence of the three allowed fine structure lines expected for the high-spin Co^{2+} state (s = 3/2) we ascribe the observed EPR spectra to the low-spin Co^{2+} state (s = 1/2). Therefore the ions are predominantly in the lowest Kramers doublet. Interestingly, hyperfine splitting is absent in our samples (Co nuclear has spin I = 7/2). This fact can be due to very broad line-width of the EPR signal that in turn is caused by very short spin-lattice relaxation times, which broaden the lines considerably. We can also distinguish less intensive features in the EPR spectra at $H_{1i} \approx 1200$ with $g_{1i} = 5.8$, at $H_{2i} \approx 3350$ G with $g_{2i} = 2.045$, at $H_{3i} \approx 4200$ G with $g_{3i} = 1.3$ and at $H_{1s} \approx 1200$ with $g_{1s} = 5.8$, at $H_{2s} \approx 1620$ G with $g_{2s} = 4.1$, at $H_{3s} \approx 3350$ G with $g_{3s} = 2.045$, which can be attributed to interstitial and substitutional Co^{2+} defects, respectively, being obviously in the thin surface layer of the SnO_2 structure [28]. The calculated spin concentrations N_s in the *Co5Sn750* and *Co10Sn750* nanocomposites are N_s(*Co5Sn750*) = $1.7*10^{20}$ spin/g and N_s(*Co10Sn750*) = $2.3*10^{20}$ spin/g, which correspond to 1.7 ± 0.3 and 2.3 ± 0.3 Co wt.%. Therefore, Co^{2+} centers represent 100 % and 60 % of total cobalt atoms in samples *Co5Sn750* and *Co10Sn750*, respectively.

The illumination of *Co5Sn750* nanocomposite directly in the cavity of the EPR spectrometer leads to insignificant change (in the range of experimental error) of EPR signal intensity. Contrarily, the spectrum of the illuminated *Co10Sn750* sample has a noticeably higher EPR signal (Fig. 7b). In the latter, the concentration of Co^{2+} centers increases up to $3.8*10^{20}$ spin/g that corresponds to 3.7 ± 0.5 Co wt.% and matches with the total cobalt content in this sample. Note that the generation of electron-hole pairs takes place during illumination of the samples. Therefore we can explain the obtained results as follows. Co_3O_4 possesses the normal spinel structure $A[B_2]O_4$ with Co^{3+} occupying the octahedral (or *B*) sites. The most interesting fact is that all cobalt ions are in the low spin state [31]. So Co^{3+} are diamagnetic centers, which are not visible in EPR, but can trap photogenerated electrons and turn into paramagnetic Co^{2+}. Such mechanism of additional Co^{2+} states appearance is evidenced by the invariance of their *g*–factor value (i.e. the electronic configuration of the spin center does not change). The

difference in concentration of paramagnetic Co^{2+} centers obtained under illumination and in dark conditions allows us to calculate the concentration of Co^{3+} in our samples. Therefore, apart from the spin Co^{2+} states, there are non-paramagnetic Co^{3+} states (about 1.5 ± 0.2 Co wt.%) in *Co10Sn750* sample. The ratio of Co^{2+} and Co^{3+} concentrations $[Co^{2+}]/[Co^{3+}] = 2.3{:}1.5 \approx 3{:}2$ while in Co_3O_4 phase $[Co^{2+}]/[Co^{3+}] = 1{:}2$. So ⅔ of Co^{2+} present in *Co10Sn750* nanocomposite is not included in the Co_3O_4 phase detected by XRD in this sample. In the *Co5Sn750* sample non-paramagnetic Co^{3+} states are probably absent, and there is no change in spin concentration under illumination.

3.3 Phase analysis

Fig. 8 shows the X-ray powder diffraction patterns of the *CoXSn300* (Fig. 8a), and *CoXSn750* (Fig. 8b). In the XRD pattern of the *Co10Sn750* nanocomposite, diffraction peaks corresponding to the Co_3O_4 phase can be found. Slight asymmetric broadening to the left side of the peak at $2\Theta = 37.5^o$ in the diffraction pattern of the *Co10Sn300* sample may be due to the presence of a cobalt oxide phase. The Co_3O_4 (ICDD 42-1467) and CoO (ICDD 42-1300) phases have the most intensive peaks at $2\Theta = 36.85^o$ and $2\Theta = 34.15^o$, respectively. Considering the XPS data, it should be assumed that in this case the phase formed is cobalt (II) oxide CoO. All nanocomposites *CoXSn300* and *CoXSn750* with lower cobalt content contain only one crystalline phase, i.e. SnO_2 (cassiterite). The phase composition and average crystallite size (d_{XRD}) of SnO_2 and Co_3O_4 phases determined from XRD spectra are shown in Table 1. For *CoXSn300* nanocomposites an increase in cobalt content gives rise to SnO_2 grain size reduction as estimated from the peak broadening in XRD spectra. That correlates with a rise of specific surface area of these samples (Table 1).

The lattice parameters of SnO_2 in the *CoXSn300* and *CoXSn750* nanocomposites have been determined from the X-ray diffraction patterns (Fig. 9). The change of lattice parameters correlates with cobalt distribution in the SnO_2 matrix (Table 1). For *CoXSn750* nanocomposites no change of SnO_2 lattice parameters is observed. This is consistent with the results of ICP-MS analysis, which showed that these samples do not contain cobalt in SnO_2 bulk (cobalt is located on the surface of SnO_2 crystallites).

For the *Co10Sn300* sample, on the contrary, an increase in *a* and *c* parameters of the SnO_2 lattice was found (Fig. 9). The total cobalt concentration in this sample is 4.8 wt.%, while the surface cobalt content is only 1.8 wt.%. Thus the *Co10Sn300* sample contains about 3 wt.% cobalt in the SnO_2 bulk. A growth in SnO_2 lattice parameters may indicate the formation of a solid solution, in which larger Co^{2+} cations (r = 0.74 Å in high spin configuration in oxygen octahedral environment [32]) replace Sn^{4+} cations (r = 0.69 Å in oxygen octahedral environment [32]) in regular positions of the SnO_2 structure. The remaining part of cobalt, which is not included in the crystalline structure of SnO_2, apparently forms a segregation of amorphous oxide phase on the surface of the tin dioxide grains. Joint consideration of the results obtained by XPS, EPR, and XRD methods, leads to the conclusion that in the samples, in which the Co_3O_4 crystalline phase is not detected by X-ray diffraction, cobalt is present only in the +2

oxidation state, being in the SnO_2 based solid solution or/and in the form of segregation on the surface of SnO_2 grains as amorphous phase CoO.

This segregation leads to the decrease of $d_{XRD}(SnO_2)$ with the growth of cobalt content in *CoXSn300* nanocomposites (Table 1). This trend has general character and was observed for different nanocrystalline materials in form of powders [3] and thin films [33,34]. The presence of impurities on the surface of the growing crystallites slows their growth under the isothermal annealing [35]. This reducing of the crystallite size with the volume fraction of the amorphous phase segregated on their surface is described by a power law [36].

3.5 Electrical and gas sensor properties

The increase in cobalt content results in a significant growth of nanocomposites resistivity (Fig. 10). This tendency is observed for both series of samples. However, in these nanocomposites cobalt exists in different locations depending on synthesis conditions. It can occupy the metal sites in the SnO_2 crystal structure forming the substitution defects Co_{Sn}, which act in SnO_2 as acceptor centers [37]. Besides this, cobalt atoms form a segregation of amorphous or crystalline CoO_x phase on the surface of SnO_2 grains. So, the resistivity growth can be explained by a decrease in charge carriers concentration, an increase in surface barriers between SnO_2 grains, and $p - n$ junction formation. The SnO_2 lattice doping with acceptor impurity Co_{Sn} leads to the compensation of intrinsic donor defects, which are oxygen vacancies. This declines the charge concentration, enlarging the thickness W of the space charge region (SCR) determined by the Debye length L_D and band bending V_s induced by oxygen chemisorption:

$$W = L_D \sqrt{\frac{eV_s}{kT}}, L_D = \sqrt{\frac{\varepsilon\varepsilon_0 kT}{e^2 n_0}}, \quad (1)$$

where n_0 is the carrier's concentration, e is the elementary charge, k is Bolzmann's constant, T is the operating temperature. The compensation effect results in a decrease in the charge concentration, which in turn leads to an additional growth in barrier height at the grain boundaries. These two factors are responsible for the resistivity increase of *CoXSn300* nanocomposites.

The possibility of p – CoO or p – Co_3O_4 formation must be taken into account for *CoXSn750* series, since it leads to the formation of an electrical barrier at the contacts between n-SnO_2 and p – CoO_x [38,39]. As a result, the bands of SnO_2 bend upward in near surface region that is accompanied by the decrease in the charge concentration and the extension of SCR strongly depleted in electrons.

The interaction between the semiconductor metal oxide with the gas phase involves physisorption and chemisorption of molecules on the oxide surface. In pure air, the main components of adsorption layer include water molecules, hydroxyl groups and chemisorbed oxygen, which can exist in the form of molecular $O^-_{2(ads)}$ and atomic $O^-_{(ads)}, O^{2-}_{(ads)}$ ions. Chemisorption of molecular oxygen from atmospheric air is accompanied by localization of conduction-band electrons on the molecules:

$$\frac{\beta}{2}O_{2(gas)} + \alpha * e^- \leftrightarrow O^{-\alpha}_{\beta(ads)}, \quad (2)$$

where $O_{2(gas)}$ is the oxygen molecule in the gas phase; $O^{-\alpha}_{\beta(ads)}$ is an atomic or molecular form of chemisorbed oxygen; α = 1 and 2 – for singly and doubly charged particles, respectively; β = 1 and 2 – for atomic and molecular form, respectively; *e* is an electron that can reach the surface, *i.e.* it has sufficient energy to overcome the barrier created by a negatively charged surface. This process results in the bending of energy bands in a thin layer near the surface of semiconductor grains and in the increase in the resistivity of *n*-type semiconductors. In the interaction of reducing gases with the surface of semiconductor oxide of *n*-type conductivity, the concentration of charge carriers in the near-surface layer of the latter increases. This effect is due to the oxidation of the molecules of the reducing gas by oxygen, chemisorbed on the surface of the material, which leads to a decrease in the surface concentration of electron acceptors. Gaseous products of the gas – solid interaction are desorbed from the surface while the chemisorbed forms of oxygen consumed during the interaction are compensated in the course of dissociative adsorption of oxygen on the surface. As a result, in pure air the conductivity of the sensor material is recovered to its initial value.

Fig. 11 illustrates the electrical response of *CoXSn300* nanocomposites to the periodical change of gas phase composition from dry air to 2 ppm H_2S/air in the temperature range of 200 – 400 °C. According to the resistance response toward reducing gases CO (10 ppm), and H_2S (2 ppm), all investigated samples behave as *n*-type semiconductors. A decrease in the electrical resistance in the presence of reducing gas could be explained by the following redox reactions:

$$\beta \cdot \mathrm{CO}_{(gas)} + \mathrm{O}^{-\alpha}_{\beta(ads)} \rightarrow \beta \cdot \mathrm{CO}_{2(gas)} + \alpha \cdot e^-, \quad (3)$$

$$\beta \cdot H_2S_{(gas)} + 3O^{-\alpha}_{\beta(ads)} \rightarrow \beta \cdot SO_{2(gas)} + \beta \cdot H_2O_{(gas)} + 3\alpha \cdot e^-, \quad (4)$$

where $CO_{(gas)}, H_2S_{(gas)}$ represent the reducing gas molecule in the gas phase, $\mathrm{O}^{-\alpha}_{\beta(ads)}$ is an atomic or molecular form of chemisorbed oxygen, $CO_{2(gas)}, SO_{2(gas)}, H_2O_{(gas)}$ are the molecules of reaction products, *e* is an electron injected into the conduction band of the semiconductor.

The dynamic sensor characteristics – response time τ^{90}_{res} and recovery time τ^{90}_{rec} are determined by the kinetics of sequential and parallel processes: target gas adsorption, surface reactions, diffusion of target gas and reaction products through the porous sensitive layer, desorption of the reaction products, which have different mechanisms and energetic characteristics. So, the values of τ^{90}_{res} and τ^{90}_{rec} depend on the number of factors – material chemical composition and structure, its chemical activity, sensing film porosity, sensor working temperature, sensor chamber volume to gas flow ratio. At the measurement temperature of 400 °C for all the samples and both CO and H_2S gases the value of τ^{90}_{res} is 90 – 120 s, and

τ_{rec}^{90} is 500 – 600 s. The decrease of working temperature increases both τ_{res}^{90} and τ_{rec}^{90} values up to 150 – 180 and 650 – 750 s, respectively. These values are very significant and, apparently, are determined by the thickness of thick films and the characteristics of their porous structure formed during sintering. Improvement of dynamic characteristics can be achieved by optimizing the geometry of the electrodes, as well as the thickness and density of the sensitive layer.

Fig. 12 compares the sensor signal to CO (10 ppm) and H_2S (2 ppm) depending on temperature and cobalt content in *CoXSn300* and *CoXSn750* nanocomposites. For *CoXSn300* series no significant influence of cobalt concentration in nanocomposites on sensor signal can be revealed. At the same time for *CoXSn750* series the opposite trends are observed in the effect of cobalt on the SnO_2 gas sensitivity in the case of CO and H_2S detection.

Such behavior should be attributed to the cobalt location in the samples. In fact, in *CoXSn300* the major part of the cobalt atoms forms the substitution defects Co_{Sn} in the SnO_2 crystal structure. The rest part of cobalt (about of 30 at. % of its total content) is present in the +2 oxidation state as CoO on the surface of the SnO_2 grains. Co in the +2 oxidation state does not exhibit pronounced oxidizing properties, and therefore the detection mechanism of H_2S and CO in both cases is mainly ascribable to the redox reaction between the target gases and chemisorbed oxygen on the SnO_2 surface. So in this series of nanocomposites cobalt only plays a role of electroactive impurity.

In samples *CoXSn750* cobalt is localized on the surface of SnO_2 grains in +2 and +3 oxidation states forming nanocrystalline *p*-Co_3O_4 and/or amorphous *p*-CoO. At equilibrium, the Fermi level of catalyst (*p*-type oxide) and *n*-SnO_2 are at the same height [40]. It is known that Co_3O_4 is catalytically active in low temperature oxidation of CO and the preferred adsorption site of CO is at the Co^{3+} sites [11]. The interaction of CO with Co_3O_4 (work function 6.1 eV, band gap 1.6 eV [39]) results in its reduction to CoO (work function 4.5 eV, band gap 2.4 eV [39]). This reduction should be accompanied by a change in the Fermi level position in cobalt oxide that consequently changes the depletion level and the band bending in SnO_2. In a detailed review [11] the high activity of Co_3O_4 in low temperature CO oxidation is explained by relatively low barriers for surface reaction and by the fact that O_2 adsorption on Co_3O_4 is never inhibited by CO as observed for all noble metals. The surface of Co_3O_4 is highly oxidized [41], with Co_3O_4 being characterized by the lowest binding energy of chemisorbed oxygen with the oxide surface [42]. Considering the catalytic activity of Co_3O_4, it can be supposed that during CO detection these molecules are directly oxidized at the surface of the Co_3O_4 particles while the SnO_2 matrix is not involved in the oxidation process. Therefore, the conduction of nanocomposite remains unaffected [40]. The contribution of this process becomes more significant with the increase in the proportion of cobalt in the +3 oxidation state. This reduces the sensor signal towards CO for *CoXSn750* nanocomposites compared to bare SnO_2.

Contrary, maximum sensor signal to H_2S rises with the cobalt concentration in *CoXSn750* nanocomposites. One can assume that there is an additional mechanism of the sensor signal formation, in which cobalt oxide is involved. It was demonstrated that Co_3O_4-based materials act as effective sorbents for low temperature gas desulfurization [12,13,43] and H_2S reduces Co_3O_4 to cobalt (II) sulfides [12]. Taking into account this interaction one can conclude that the mechanism of sensor signal formation in *p*-CoO_x/*n*-SnO_2 nanocomposites is similar to that established for *p*-CuO/*n*-SnO_2 materials:

$$Co_3O_4 + H_2S_{(gas)} + O_{2(gas)} = 3CoO + SO_{2(gas)} + H_2O_{(gas)}, \quad (5)$$

$$CoO + H_2S_{(gas)} = CoS + H_2O_{(gas)}, \quad (6)$$

A large number of cobalt sulfides with different composition and crystal structure have been reported [44]. All of them have metallic conductivity. To confirm the formation of a certain cobalt sulfide under sensor measurement conditions, an additional experiment was performed. Nanocomposite *Co10Sn750* was annealed in H_2S containing atmosphere (2 ppm in air) at 250 ^oC for 1 h, cooled to room temperature in the same gas mixture, and immediately subjected to XRD examination. Fig. 13 presents the X-ray diffraction pattern of *Co10Sn750* sample after interaction with H_2S. Comparing these data with the XRD pattern presented in Fig. 8b, one can conclude that as a result of reaction with H_2S the oxide phase Co_3O_4 disappears and a cobalt sulfide phase is formed. Phase analysis using the ICDD database (Table 4) revealed that the most probable is the formation of a cobalt deficient sulfide with hexagonal structure. The proximity of the positions of the diffraction maxima for these phases and the low intensity of the reflexes of the cobalt sulfide phase on the experimental XRD pattern do not allow us to determine unambiguously which sulfide is formed. The positions of diffraction peaks, corresponding to possible cobalt sulfide phase, are marked by arrows on Fig. 13. The diffraction maxima at $2\Theta = 35.2 – 35.5^o$ and $2\Theta = 54.1 – 54.6^o$ do not appear on the diffractogram possibly because of the overlap with intense reflexes of SnO_2 phase.

So, when *p*-CoO_x is converted to metallic cobalt sulfide on exposure to H_2S, the $p – n$ junctions between *p*-CoO_x and *n*-SnO_2 are removed, and the conductivity of nanocomposites significantly increases. Such removal of the barriers is only possible in the presence of sulfur containing reducing gases providing high selectivity of *p*-CoO_x/*n*-SnO_2 nanocomposites.

4. Conclusions

Nanocomposites CoO_x/SnO_2 based on tin oxide powders with a grain size of 7 – 20 nm have been prepared by wet chemical method, and characterized in detail using ICP-MS, XPS, EPR, XRD and HAADF-STEM with EDX-STEM mapping. The most important observed effects are: (i) the different character of the cobalt distribution between the bulk and the surface of the SnO_2 nanocrystals, which

depends on the crystallinity of the SnO_2 matrix and is determined by synthesis conditions, and (ii) the influence of cobalt location on gas sensor properties of CoO_x/SnO_2 nanocomposites.

In the samples obtained on the base of low crystalline SnO_2 (powders annealed at 300 ^oC), the major part of the cobalt atoms forms substitution defects Co_{Sn} in the SnO_2 crystal structure. In this series of nanocomposites cobalt plays a role of electroactive impurity. In nanocomposites based on high crystalline SnO_2 matrix (powders annealed at 750 ^oC), cobalt is localized on the surface of SnO_2 grains and present in +2 and +3 oxidation states forming nanocrystalline *p*-Co_3O_4 and/or amorphous *p*-CoO. Formation of the *p*-CoO_x/*n*-SnO_2 heterojunctions is responsible for the electrical properties of these nanocomposites.

For gas sensors application the most interesting are the nanocomposites, in which cobalt is localized on the surface of SnO_2 grains forming *p*-CoO_x. During CO detection, the molecules of carbon monoxide can be directly oxidized entirely at the surface of the Co_3O_4 particles. SnO_2 matrix is not involved in the oxidation process and the conduction of nanocomposite remains unaffected. This results in the decrease of sensor signal of CoO_x/SnO_2 nanocomposites compared to bare SnO_2. In the case of H_2S detection the mechanism of sensor signal formation in *p*-CoO_x/*n*-SnO_2 nanocomposites is similar to that established for *p*-CuO/*n*-SnO_2 materials: H_2S reduces Co_3O_4 to cobalt (II) sulfides that results in the removal of the *p* – *n* junction and in significant increase in the nanocomposites conductivity. Such removal of the barriers is only possible in the presence of sulfur containing reducing gases providing high selectivity of *p*-CoO_x/*n*-SnO_2 nanocomposites.

Acknowledgements

This work was supported by ERA-Net.Plus grant N 096 FONSENS. EPR experiments were performed using the facilities of the Collective Use Center at the Moscow State University.

References

[1] D.R. Miller, Sh.A. Akbar, P.A. Morris, Nanoscale metal oxide – based heterojunctions for gas sensing: A review, Sens. Actuators B 204 (2014) 250–272.

[2] V.V. Krivetskiy, M.N. Rumyantseva, A.M. Gaskov, Chemical modification of nanocrystalline tin dioxide for selective gas sensors. Russ. Chem. Rev. 82 (2013) 917–941.

[3] M.N. Rumyantseva, A.M. Gaskov, Chemical modification of nanocrystalline metal oxides: effect of the real structure and surface chemistry on the sensor properties, Russ. Chem. Bull. 57 (2008) 1086–1105.

[4] R.B. Vasiliev, M.N. Rumyantseva, L.I. Ryabova, A.M. Gaskov, Inorganic structures as materials for gas sensors, Russ. Chem. Rev. 73 (2004) 939–956.

[5] U.-S. Choi, G. Sakai, K. Shimanoe, N. Yamazoe, Sensing properties of SnO_2-Co_3O_4 composites to CO and H_2, Sens. Actuators B 98 (2004) 166–173.

[6] S. Abe, U.-S. Choi, K. Shimanoe, N. Yamazoe. Influence of ball-milling time on gas-sensing properties of Co_3O_4-SnO_2 nanocomposites, Sens. Actuators B 107 (2005) 516–522.

[7] L. Liu, Ch. Guo, Sh. Li, L. Wang, Q. Dong, W. Li, Improved H_2 sensing properties of Co-doped SnO_2 nanofibers, Sens. Actuators B 150 (2010) 806–810.

[8] L.P. Oleksenko, N.P. Maksymovych, A.I. Buvailo, I.P. Matushko, N. Dollahon, Adsorption – semiconductor hydrogen sensors based on nanosized tin dioxide with cobalt additives, Sens. Actuators B 174 (2012) 39–44.

[9] G. Korotcenkov, I. Boris, V. Brinzari, S.H. Han, B.K. Cho, The role of doping effect on the response of SnO_2-based thin film gas sensors: Analysis based on the results obtained for Co-doped SnO_2 films deposited by spray pyrolysis, Sens. Actuators B 182 (2013) 112–124.

[10] S.B. Patil, P.P. Patil, M.A. More, Acetone vapour sensing characteristics of cobalt-doped SnO_2 thin films, Sens. Actuators B 125 (2007) 126–130.

[11] S. Royer, D. Duprez, Catalytic oxidation of carbon monoxide over transition metal oxides, ChemCatChem 3 (2011) 24–65.

[12] T. Baird, K.C. Campbell, P.J. Holliman, R.W. Hoyle, M. Huxam, D. Stirling, B.P. Williams, M. Morris, Cobalt–zinc oxide absorbents for low temperature gas desulfurization, J. Mater. Chem. 9 (1999) 599–605.

[13] L.R. Pahalagedara, A.S. Poyraz, W. Song, Ch.-H. Kuo, M.N. Pahalagedara, Yo.-T. Meng, S.L. Suib, Low Temperature Desulfurization of H_2S: High Sorption Capacities by Mesoporous Cobalt Oxide via Increased H_2S Diffusion, Chem. Mater. 26 (2014) 6613–6621.

[14] Q. Wang, X. Li, F. Liu, Ya. Sun, Ch. Wang, X. Li, P. Sun, J. Lin, G. Lu, Three-dimensional flake-flower Co/Sn oxide composite and its excellent ethanol sensing properties, Sens. Actuators B 230 (2016) 17-24.

[15] L. Wang, Zh. Lou, R. Zhang, T. Zhou, J. Deng, T. Zhang, Hybrid Co_3O_4/SnO_2 Core-Shell Nanospheres as Real-Time Rapid-Response Sensors for Ammoinia Gas, ACS Appl. Mater. Interfaces 8 (2016) 6539-6545.

[16] H.-M. Jeong, J.-H. Kim, S.-Yo. Jeong, Ch.-H. Kwak, J.-H. Lee, Co_3O_4-SnO_2 hollow hetero-nanostructures: Facile control of gas selectivity by compositional tuning of sensing materials via galvanic replacement, ACS Appl. Mater. Interfaces 8 (2016) 7877-7883.

[17] S.-Yo. Jeong, J.-W. Yoon, T.-H. Kim, H.-M. Jeong, Ch.-S. Lee, Yu. Ch. Kang, J.-H. Lee, Ultra-selective detection of sub-ppm-level benzene using Pd-SnO_2 yolk-shell micro-reactors with a catalytic Co_3O_4 overlayer for monitoring air quality, J. Mater. Chem. A 5 (2017) 1446-1454.

[18] Sh. Bai, H. Liu, A. Chen, D. Li, SnO_2@Co_3O_4 p-n heterostructures fabricated by electrospinning and mechanism analysis enhanced acetone sensing, RSC Adv. 4 (2014) 62862-62868.

[19] X. Kou, Ch. Wang, M. Ding, Ch. Feng, X. Li, J. Ma, H. Zhang, Ya. Sun, G. Lu, Synthesis of Co-doped SnO_2 nanofibers and their enhanced gas-sensing properties, Sens. Actuators B 236 (2016) 4225-432.

[20] Yo.J. Kwon, H.G. Na, S.Yo. Kang, M.S. Choi, J.H. Bang, T.W. Kim, A. Mizraei, H.W. Kim, Attachment of Co_3O_4 layer to SnO_2 nanowires for enhanced gas sensing properties, Sens. Actuators B 239 (2017) 180-192.

[21] L. Huo, X. Yang, Z. Liu, X. Tian, T. Qi, X. Wang, K. Yu, J. Sun, M. Fan, Modulation of potential barrier heights in Co_3O_4/SnO_2 heterojunctions fot highly H_2-selective sensors, Sens. Actuators B 244 (2017) 694-700.

[22] J.-H. Kim, J.-H. Lee, A. Mizraei, H.W. Kim, S.S. Kim, Optimization and gas sensing mechanism of n-SnO_2-p-Co_3O_4 composite nanofibers, Sens. Actuators B 248 (2017) 500-511.

[23] M.N. Rumyantseva, A.M. Gaskov, N. Rosman, T. Pagnier, J.R. Morante, Raman surface vibration modes in nanocrystalline SnO_2 prepared by wet chemical methods: correlations with the gas sensors performances, Chem. Mater. 17 (2005) 893–901.

[24] C.D. Wagner, W.M. Riggs, L.E. Davis, G.F. Moulder, Handbook of X-ray Photoelectron Spectroscopy, Perkin Elmer Co, 1979.

[25] M. Batzill, T. James, M. Burst, U. Diebold, Pure and cobalt-doped SnO_2(101) films grown by molecular beam epitaxy on Al_2O_3, Thin Solid Films 484 (2005) 132–139.

[26] T.J. Chuang, C.R. Brundle, V. Rice, Interpretation of the X-Ray photoemission spectra of cobalt oxides and cobalt oxide surfaces, Surf. Sci. 59 (1976) 413–429.

[27] M.C. Biesinger, B.P. Payne, A.P. Grosvenor, L.W.M. Lau, A.R. Gerson, R.St.C. Smart, Resolving surface chemical states in XPS analysis of first row transition metals, oxides and hydroxides: Cr, Mn, Fe, Co and Ni, Appl. Surf. Sci. 257 (2011) 2717–2730.

[28] S.K. Misra, S.I. Andronenko, K.M. Reddy, J. Hays, A. Punnoose, Magnetic resonance studies of Co^{2+} ions in nanoparticles of SnO_2 processed at different temperatures, J. Appl. Phys. 99 (2006) 08M106-1–08M106-3.

[29] S. Angelov, E. Zhecheva, R. Stoyanova, M. Atanasov, Bulk defects in Co_3O_4, pure and slightly doped with lithium, revealed by EPR of the tetrahedral Co^{2+} ions, J. Phys. Chem. Sol. 51 (1990) 1157–1161.

[30] P. Dutta, M.S. Seehra, S. Thota, J. Kumar, A comparative study of the magnetic properties of bulk and nanocrystallineCo_3O_4, J. Phys.: Condens. Matter 20 (2008) 015218-1–015218-8.

[31] W.L. Smith, A.D. Hobson, The structure of cobalt oxide Co_3O_4, Acta Cryst. B 29 (1973) 362–363

[32] R.D. Shannon, Revised Effective Ionic Radii and Systematic Studies of Interatomic Distances in Halides and Chalcogenides, Acta. Cryst. A 32 (1976) 751–767.

[33] M.N. Rumyantseva, O.V. Safonova, M.N. Boulova, L.I. Ryabova, A.M. Gaskov, Dopants in nanocrystalline tin dioxide, Russ. Chem. Bull., Int. Ed. 52 (2003) 1217–1238.

[34] N.A. Vorobyeva, M.N. Rumyantseva, R.B. Vasiliev, V.F. Kozlovskiy, YuM. Soshnikova, D.G. Filatova, V.B. Zaytsev, A.V. Zaytseva, A.M. Gaskov, Doping effects on electrical and optical properties of spin-coated ZnO thin films, Vacuum 114 (2015) 198–204.

[35] M. Miodownik, E.A.Holm, G.N. Hassold, Highly parallel computer simulation of particle pinning: Zener vindicated, Scripta Mater. 42 (2000) 1173–1177.

[36] Z.-J. Liu, Y.G.Shen, Effects of amorphous matrix on the grain growth kinetics in two-phase nanostructured films: a Monte Carlo study, Acta Mater. 52 (2004) 729–736.

[37] M.N. Rumyantseva, A.M. Gaskov, L.I. Ryabova, J.P. Senateur, B. Chenevier, M. Labeau, Pyrosol spraying deposition of copper- and nickel-doped tin oxide films, Mater. Sci. Eng. B 41 (1996) 333–338.

[38] T. Minami, T. Miyata, T.Yamamoto, Work function of transparent conducting multicomponent oxide thin films prepared by magnetron sputtering, Surf. Coat. Technol. 108 (1998) 583–587.

[39] M.T. Greiner, M.G. Helander, W.-M. Tang, Zh.-B. Wang, J. Qiu, Zh.-H. Lu, Universal energy-level alignment of molecules on metal oxides, Nature Mater. 11 (2011) 75–81.

[40] A. Gurlo, N. Bârsan, U. Weimar. Gas Sensors Based on Semiconducting Oxides. In Metal Oxides: Chemistry and Applications (Ed. J.L.C. Fierro). Ch. 22. pp. 683 – 738.

[41] G. Busca, R. Guidetti, V. Lorenzelli, Fourier-transform Infrared Study of the Surface Properties of Cobalt Oxides, J. Chem. Soc. Faraday Trans.86 (1990) 989–994.

[42] V.A. Razdobarov, V.A. Sadykov, S.A. Veniaminov, N.N. Bulgakov, O.N. Kovalenko, Yu.D. Pankratiev, V.V. Popovskii, G.N. Kryukova, S.F. Tikhov, Nature of the active oxygen of Co_3O_4, React. Kinet. Catal. Lett. 37 (1988) 109 – 114.

[43] S.W. Chun, J.Ye. Jang, D.W. Park, H.Ch.Woo, J.S.Chung, Selective oxidation of H_2S in the presence of ammonia and water using Co_3O_4/SiO_2 catalyst, Kor. J. Chem. Eng. 14 (1997) 216–218.

[44] N.N. Greenwood and A. Earnshaw, Cobalt, Rhodium and Iridium. In Chemistry of the Elements, Elsevier Science Ltd.: Kidlington, 1997.

Table 1. Samples designation, composition and microstructure parameters.

Sample	Preassigned, [Co]/([Co]+[Sn])	Co content, wt. %		Phase composition	d_{XRD}, nm[a]	S_{BET}, m^2/g[b]
	at.%	Total	Surface			
Sn300	-	-	-	SnO_2	7 ± 1	40 ± 5
Co1.5Sn300	1.5	0.47 ± 0.03	0.14 ± 0.01	SnO_2	7 ± 1	40 ± 5
Co5Sn300	5	2.1 ± 0.2	0.82 ± 0.06	SnO_2	5.5 ± 0.5	55 ± 5
Co10Sn300	10	4.8 ± 0.3	1.8 ± 0.2	SnO_2	5.0 ± 0.5	60 ± 5
Sn750	-	-	-	SnO_2	16 ± 1	8 ± 5
Co1.5Sn750	1.5	1.15± 0.09	1.05 ± 0.09	SnO_2	16 ± 1	9 ± 5
Co5Sn750	5	1.8 ± 0.1	1.6 ± 0.1	SnO_2	20 ± 2	9 ± 5
Co10Sn750	10	3.9 ± 0.3	3.8 ± 0.3	SnO_2,	21 ± 2	12 ± 5
				Co_3O_4	10 ± 2	

[a]Average crystallite size estimated using Scherrer equation. [b]Specific surface area.

Table 2. Crystallographic planes in *Co10Sn300* and *Co10Sn750* samples.

$d_{observed}$, Å		SnO_2		Co_3O_4	
Co10Sn300	*Co10Sn750*	d, Å	(hkl)	d, Å	(hkl)
3.36	3.35	3.347	(101)		
2.64	2.64	2.643	(110)		
	2.45	---	---	2.437	(311)
2.34	2.36	2.369	(200)		
	2.29	2.309	(111)		
	2.11	2.119	(210)		
1.76	1.76	1.764	(211)		
	1.67	1.675	(220)		
	1.59	1.593	(002)		
	1.50	1.498	(310)		
1.43	1.44	1.439	(112)		
	1.41	1.416	(301)		

Table 3. Co $2p_{3/2}$ XPS spectral assignments

	Co $2p_{3/2}$ binding energy (eV)					
	Reference data		Sample			
Spectral assignment	Ref. 24	Ref. 25	Co10Sn750	Co10Sn300	Co1.5Sn750	Co1.5Sn300
Co(III) Co_3O_4	779.6	779.6	780.0			
Co(II) Co_3O_4	780.7	780.9, 782.2	782.3			
Co(II) CoO	780.5	780.0, 782.1		781.7	780.7	781.0
Co(II)ss CoO[a]	786.4	786.5	786.9	787.0	785.4	
Co(II)ss Co_3O_4[b]	789.5	789.5	790.5			
separation of the Co $2p_{1/2}$–$2p_{3/2}$ spin orbit components, eV			15.2	15.5	15.8	-

[a]Shake-up satellite of Co(II) in CoO structure. [b]Shake-up satellite of Co(II) in Co_3O_4 structure.

Table 4. Positions of diffraction maxima in XRD patterns of cobalt sulfides.

XRD pattern	Diffraction angle 2Θ, ° (λ = 1.5406 Å)			
Co10Sn750 sample annealed in air containing 2 ppm H_2S	30.67	-	46.66	-
ICDD 19-366 $CoS_{1.097}$ (hexagonal, *P63/mmc*)	30.906 20[a]	35.554 35[a]	47.020 100[a]	54.617 55[a]
ICDD 25-1081 $CoS_{1.035}$ (hexagonal, *P63/mmc*)	30.474 20[a]	35.265 20[a]	46.662 100[a]	54.094 35[a]
ICDD 42-826 $Co_{1-x}S$, $x = 0.9$ (hexagonal, *P63/mmc*)	30.517 60[a]	35.179 70[a]	46.764 100[a]	54.267 45[a]

[a] Relative intensity

Figure 1: HAADF-STEM images of (a) *Co10Sn300* and (b) *Co10Sn750* samples.

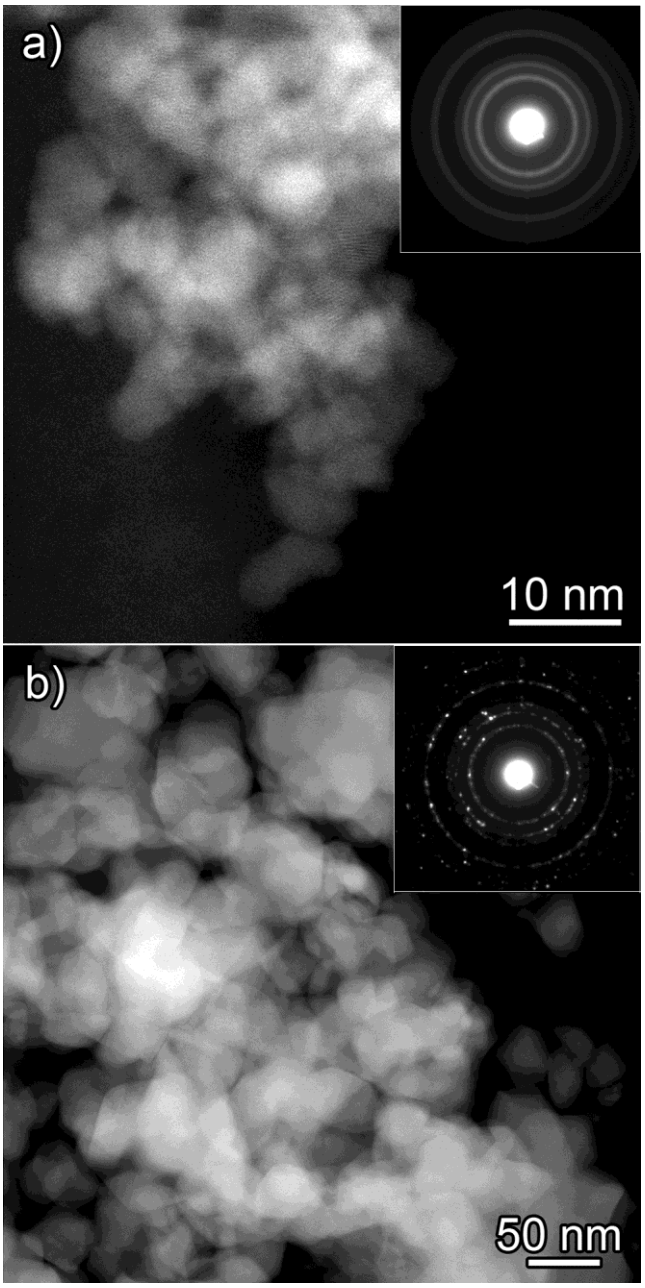

Figure 2: HAADF-STEM image and EDX-STEM maps of *Co10Sn300* sample.

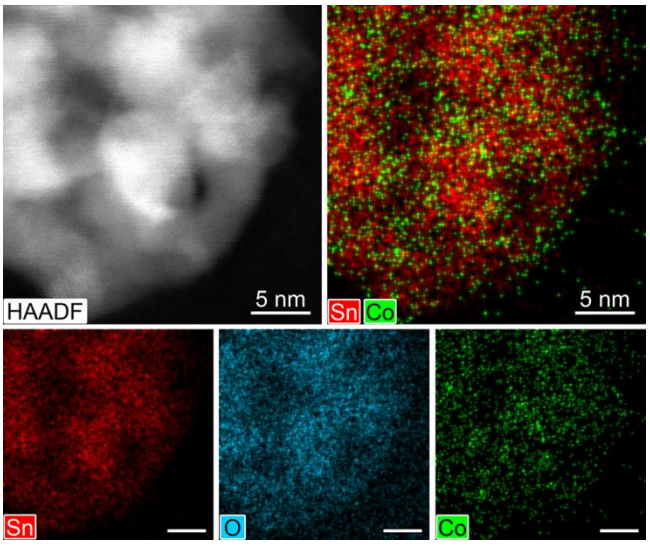

Figure 3: HAADF-STEM image and EDX-STEM maps of *Co10Sn750* sample.

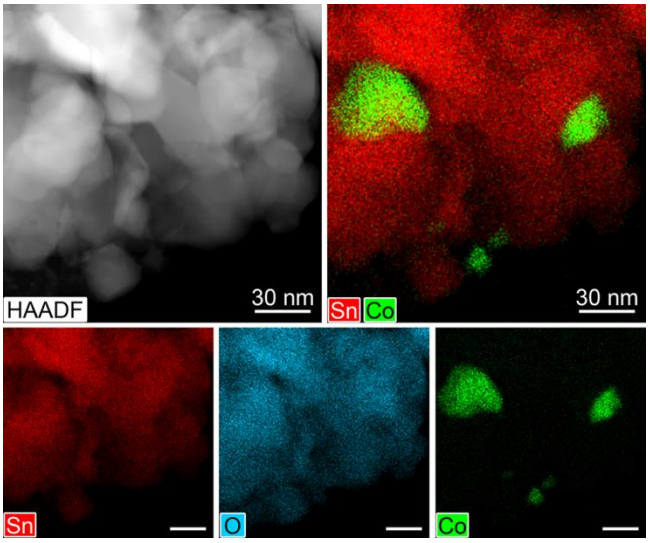

Figure 4: Co content (wt. %) on the surface of SnO_2 grains *vs*. its total amount (wt. %) in *CoXSn300* and *CoXSn750* nanocomposites. Dash line illustrates the situation when all cobalt atoms are located on the surface of SnO_2 grains.

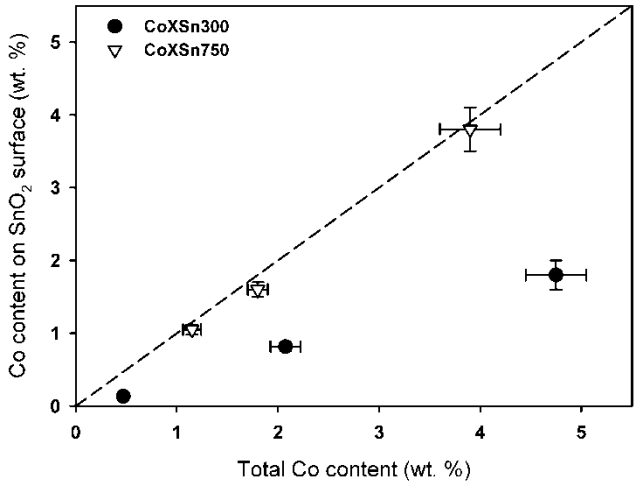

Figure 5: XP survey spectrum of *Co10Sn750* nanocomposite. Insets: left – O 1s spectrum, right – Sn 3d spectrum.

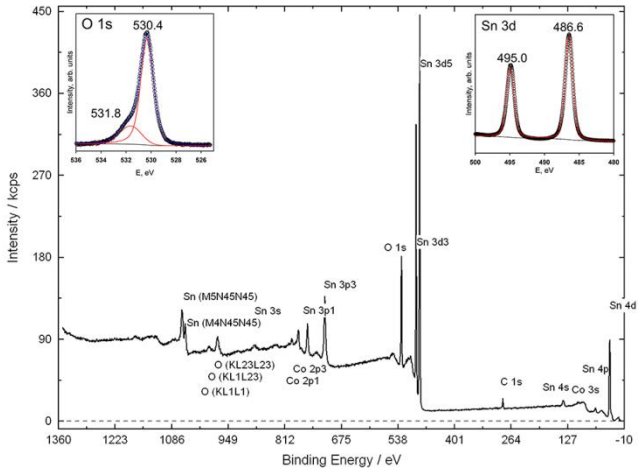

Figure 6: Co 2p XP-spectra fitted by 2 or 4 doublets corresponding to Co(III) (black) and Co(II) (red) main peaks and Co(II) shake-up satellites, corresponding to Co_3O_4 (green) and CoO (pink) environment.

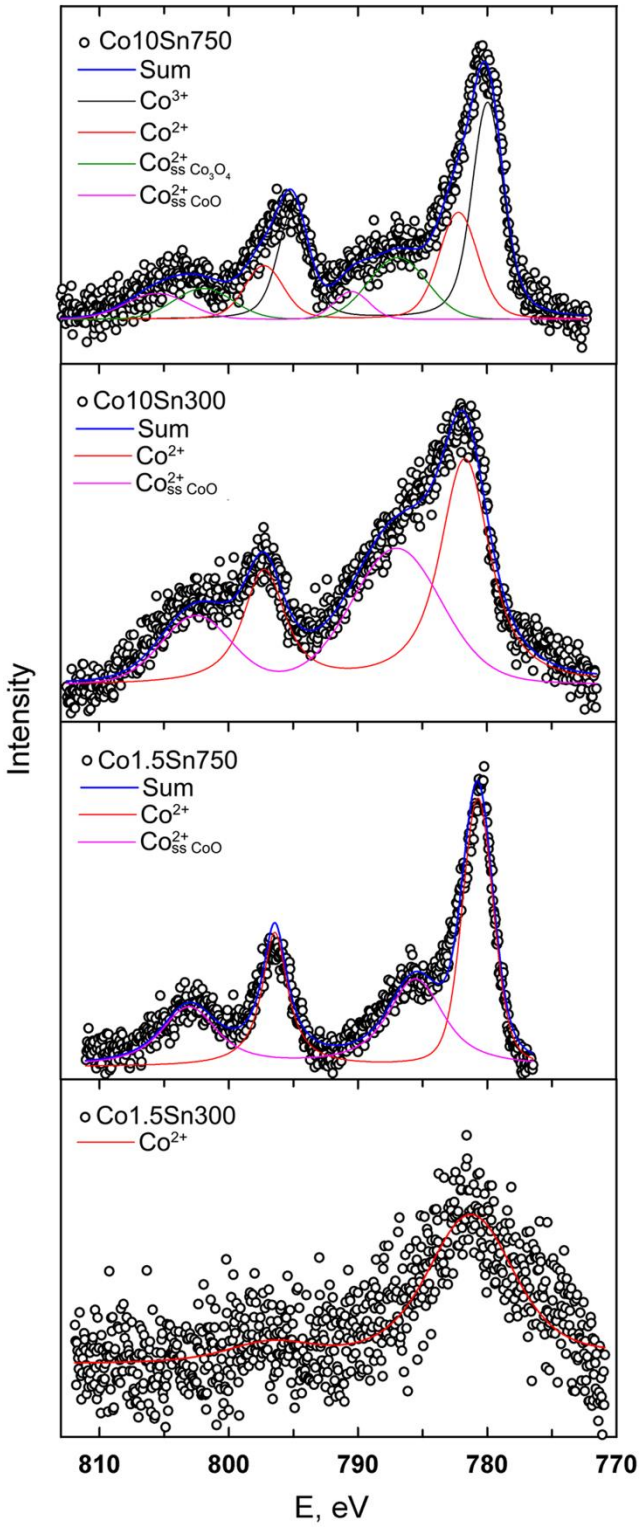

Figure 7: (a) EPR spectra (dark) of *Co5Sn750* and *Co10Sn750* nanocomposites. (b) EPR spectra of *Co10Sn750* nanocomposite in dark conditions and under illumination.

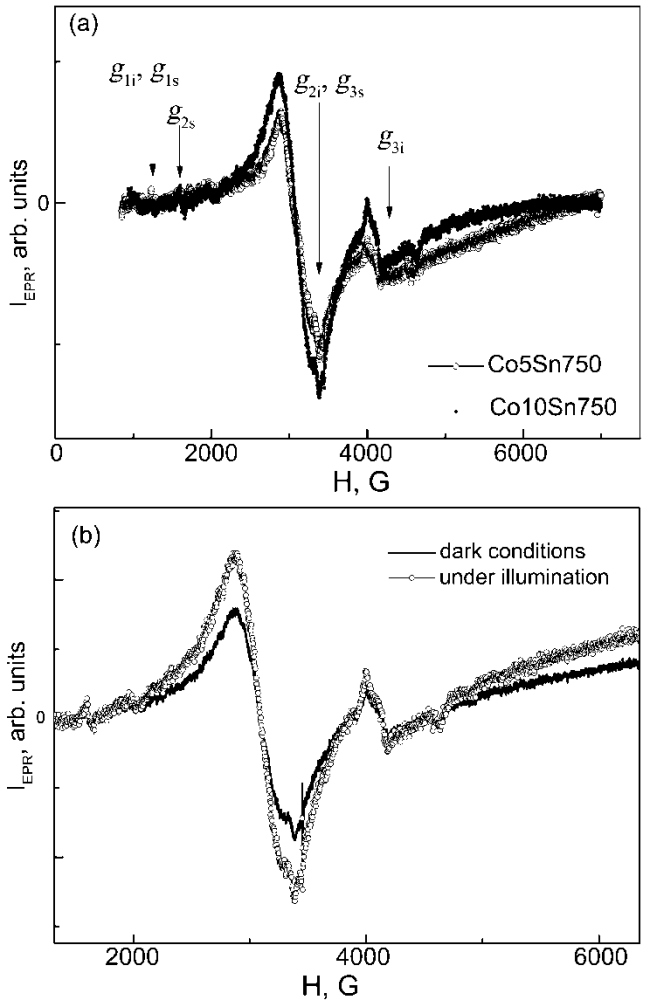

Figure 8: X-ray diffraction patterns of the *CoXSn300* (a) and *CoXSn750* (b) nanocomposites. Dot and dash-dot lines correspond to the reflection positions of SnO_2 and Co_3O_4, respectively.

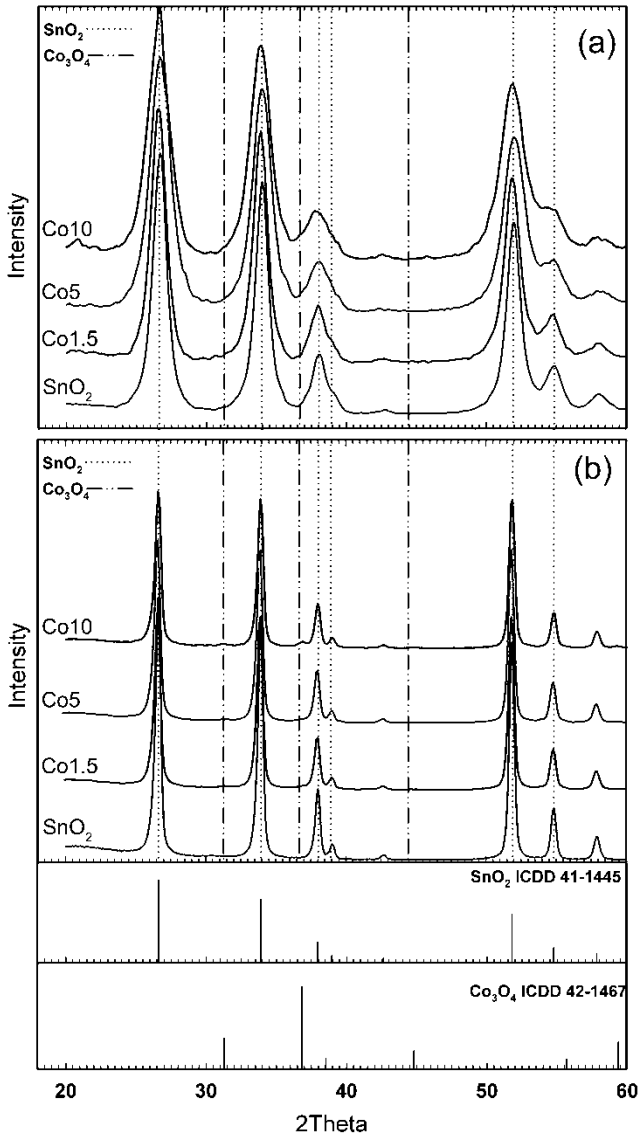

Figure 9: SnO_2 lattice parameters in *CoXSn300* and *CoXSn750* nanocomposites. Dashed lines correspond to the parameters values from ICDD 41-1445 (SnO_2 cassiterite).

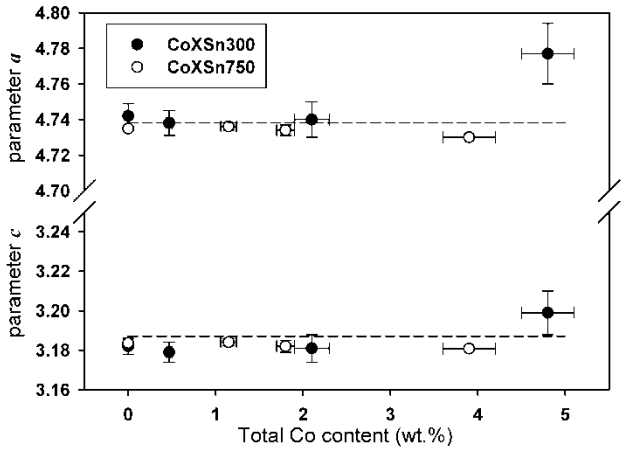

Figure 10: Samples resistance measured in dry air at 200°C.

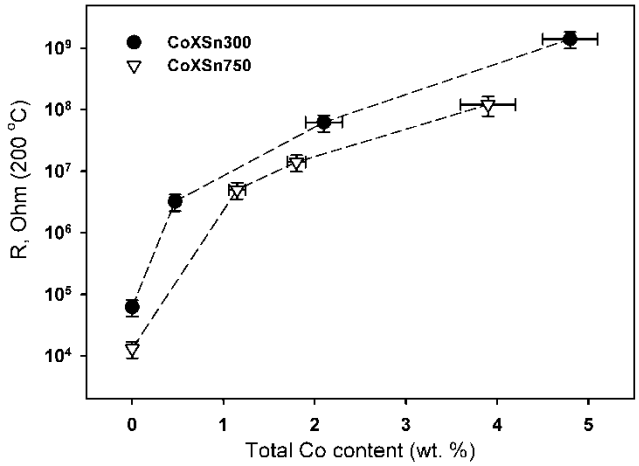

Figure 11: Electrical response of *CoXSn300* nanocomposites to the periodical change of gas phase composition from dry air (15 min) to 2 ppm H_2S/air (15 min) in the temperature range 200 – 400 °C. (1) – SnO_2, (2) – Co1.5Sn300, (3) – Co5Sn300, (4) – Co10Sn300.

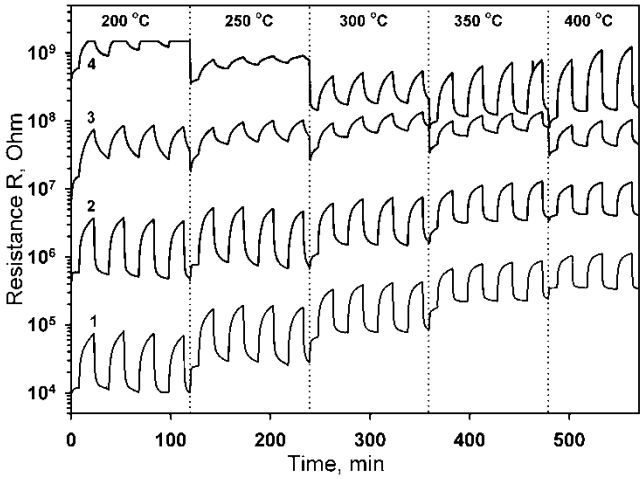

Figure 12: Sensor signal to CO (10 ppm) and H_2S (2 ppm) depending on temperature and cobalt content in *CoXSn300* and *CoXSn750* nanocomposites.

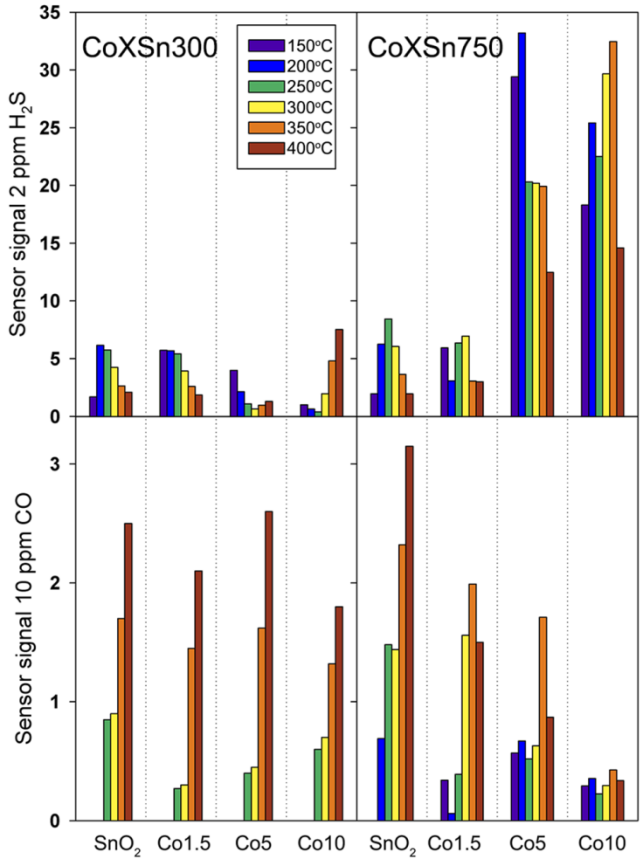

Fig. 13: X-ray diffraction patterns of *Co10Sn750* nanocomposite after interaction with H_2S. Arrows indicate the positions of cobalt sulfide diffraction peaks. Asterisks denote SnO_2 diffraction peaks.